separations

MDPI

Article

A Comprehensive Physicochemical Assessment on Cyclic Stability and High-Capacity CO_2 Sorption Performance in Amine-Tethered Polymeric Resin

Ahmad Mohammad Rasheed Al-Bodour [1], Nimarta Kaur [1], Alberto Gutiérrez Vega [2], Santiago Aparicio [2] and Mert Atilhan [1,*]

[1] Chemical and Paper Engineering Department, Western Michigan University, Kalamazoo, MI 49008-5462, USA; a.al-bodour@wmich.edu (A.M.R.A.-B.); nimarta.kaur@wmich.edu (N.K.)
[2] Department of Chemistry, University of Burgos, 09001 Burgos, Spain; agvega@ubu.es (A.G.V.); sapar@ubu.es (S.A.)
* Correspondence: mert.atilhan@wmich.edu

Abstract

The urgent need for effective carbon dioxide (CO_2) mitigation strategies necessitates the development of robust, high-capacity sorbents for CO_2 separation processes that operate from sub-atmospheric to elevated pressures. This study systematically evaluates the structural, thermodynamic, and gravimetric performance of a commercial amine-functionalized macroporous polymer resin (LEWATIT VP OC 1065). The sorbent demonstrated a maximum CO_2 uptake of 2.76 mmol/g at 20 °C and 1 bar, scaling to an exceptional capacity of 4.65 mmol/g at 30 bar. A dedicated nitrogen N_2 adsorption and desorption experiment at 20 °C yielded a CO_2 to N_2 selectivity between approximately 74 and 97 across the 100 to 1000 mbar window, confirming that the balance N_2 of air or flue gas feeds does not compete measurably for capacity. Thermodynamic assessments indicate that chemisorption dictates uptake at low partial pressures, while physisorption mechanisms contribute at elevated pressures. A dual-site Langmuir model with shared site capacities of 1.87 and 1.70 mmol/g describes the three absolute isotherms with $R^2 \geq 0.997$. The measured isotherms give working capacities of 0.45 to 0.85 mmol/g for a 1000 to 100 mbar pressure swing and 2.1 mmol/g for a 30 to 1 bar swing at 20 °C. Furthermore, cyclical adsorption–desorption evaluations confirmed sustained capture efficiency and structural resilience over 20 continuous cycles utilizing thermal-vacuum regeneration. All measurements were performed with pure CO_2 under dry conditions. The results therefore constitute a sorbent-level equilibrium and kinetic assessment. These findings support this aminated resin as a versatile and stable candidate for a wide operational spectrum of CO_2 separation applications and provide the thermodynamic and kinetic dataset required for isotherm model fitting and process simulation.

Keywords: CO_2 capture; amine-functionalized resin; magnetic suspension balance; adsorption thermodynamics; high-pressure adsorption; cyclic stability

Check for updates

Academic Editor: Guojie Zhang

Received: 22 October 2026
Revised: 13 November 2026
Accepted: 15 November 2026
Published: 18 November 2026

Copyright: © 2026 by the authors. Licensee MDPI, Basel, Switzerland. This article is an open access article distributed under the terms and conditions of the Creative Commons Attribution (CC BY) license.

1. Introduction

CO_2 gas is the most significant gas among the greenhouse gases. The emissions of CO_2 contribute significantly to global warming [1]. Global CO_2 emissions are projected to reach 36.34 gigatons annually. This is due to the continued rise in demand for fossil fuels. In accordance with the Intergovernmental Panel on Climate Change (IPCC), hundreds of gigatons of CO_2 must be removed before 2050. This is to follow the route of 1.5 °C with no

or limited overshoot [2]. Limiting global warming and achieving net-zero emissions of CO_2 requires capture at point sources together with removal of CO_2 from the atmosphere [3]. Direct air capture (DAC), a concept established by Lackner in the 1990s [4], has reached first commercial implementations [5,6]. CO_2 capture technologies are categorized according to the mechanism of separation into four classifications: physical adsorption, chemical adsorption, chemical absorption, and electrochemically mediated CO_2 capture (EMCC) [7]. The analysis of the open literature over the previous decade shows that the adsorption technologies employing porous materials like activated carbon, metal–organic frameworks (MOFs), and nano-fibrillated cellulose experienced quick advancement [8,9].

Point source capture targets specific points of emission, while DAC offers supplementary paths for a larger scale of carbon removal. Pressurized streams such as biogas, pre-combustion syngas, and natural gas add a third application window above 1 bar. The integration of these technologies allows for broader methods to accomplish negative emissions targets and mitigation of CO_2 accumulation impact in the atmosphere [10]. Low et al. reviewed over 200 materials that were proposed as adsorbents for DAC applications. These include metal oxides, silicas, zeolites, MOFs, and polymers [11]. Several metrics reported values of CO_2 uptake by adsorbents at 0.04 kPa and a single-temperature isotherm typically 25 °C. Nevertheless, research works by Rajagopalan et al. [12], Khurana and Farooq [13], and Farmahini et al. [14] showed that such simple metrics are insufficient for screening the adsorbents. Process-based screening requires full isotherms at several temperatures, including the desorption branch, together with kinetic and cyclic data. Bos et al. studied the effect of water co-adsorption and steam purge on CO_2 adsorption by LEWATIT VP OC 1065 at 20 °C temperature and regeneration at 91 and 116 °C using fixed-bed reactor. The maximum capacity reported was 1.6 mmol/g at 910 mbar pressure with an uncertainty of ~+0.1 mmol/g [15].

Among solid chemisorbents, amine-functionalized materials occupy a central position because the acid–base chemistry between amine groups and CO_2 provides the steep, high-affinity isotherms required to capture CO_2 at low partial pressures [5,11]. The material studied in this work, LEWATIT VP OC 1065, is a macroporous polystyrene–divinylbenzene resin bearing primary benzylamine groups with N_2 content of 6.7 to 7.5 mol N/kg [16,17], and it has emerged as a benchmark sorbent for CO_2 capture studies. Alesi and Kitchin provided an early evaluation of this resin for CO_2 capture [18]. Veneman et al. quantified its CO_2 and H_2O uptake, reporting approximately 2.8 mol/kg of CO_2 at 303 K under concentrated CO_2 together with an isosteric heat of adsorption between 75 and 87 kJ/mol, and observed that co-adsorbed water enhances rather than suppresses the CO_2 capacity through bicarbonate forming pathways [16]. Yu et al. mapped the degradation landscape of the same resin, establishing thermal stability below 150 °C in inert atmosphere, urea formation in concentrated CO_2 above approximately 120 °C, oxidative degradation above approximately 70 °C in air, and notable steam stability attributed to the carbon–carbon anchoring of the benzylamine groups to the polystyrene backbone [19]. Buijs and de Flart elucidated the capture mechanism computationally, identifying water-assisted carbamic acid formation, with a reaction enthalpy of −75.6 kJ/mol, as the energetically preferred pathway [17]. Sonnleitner et al. assessed the resin against zeolite 13X for continuous temperature-swing adsorption, reporting approximately 2.5 mol/kg at 40 °C and 0.5 bar and an isosteric heat of approximately 76 kJ/mol [20]. Under dilute feeds, Chimani et al. reported breakthrough measurements at 400 ppm CO_2 under controlled relative humidity together with validated CO_2 and H_2O co-adsorption models [21].

Although previous studies have provided valuable insights into the CO_2 adsorption performance of LEWATIT VP OC 1065, including adsorption equilibria, thermodynamics, kinetics, regeneration, and material stability [15–21], these investigations have primarily

addressed specific operating conditions and individual aspects of sorbent performance. However, experimental studies investigating CO_2 adsorption at substantially elevated pressures remain limited, particularly those integrating equilibrium modeling, kinetic analysis, thermodynamic characterization, and cyclic stability assessment. This highlights a gap in the comprehensive experimental characterization of LEWATIT VP OC 1065 across a broad pressure range, especially under elevated-pressure conditions relevant to industrial CO_2 capture applications. Table 1 compares the maximum CO_2 pressures investigated in the present work with those reported in selected previous studies on LEWATIT VP OC 1065.

Table 1. Comparison of CO_2 pressure ranges investigated for LEWATIT VP OC 1065 in the present work and selected previous studies.

Material	Maximum P/bar	Reference
LEWATIT VP OC 1065	30 pure CO_2	This Work
LEWATIT VP OC 1065	0.8 CO_2	[16]
LEWATIT VP OC 1065	0.5 CO_2	[20]
LEWATIT VP OC 1065	1.01 CO_2	[19]
LEWATIT VP OC 1065	0.005 CO_2	[15]
LEWATIT VP OC 1065	1.0 CO_2	[17]
LEWATIT VP OC 1065	0.001 CO_2	[21]
LEWATIT VP OC 1065	1.0 CO_2	[22]

To address this research gap, the present study provides an integrated experimental investigation of CO_2 adsorption on LEWATIT VP OC 1065 using a high-resolution magnetic suspension balance (MSB) with a nominal mass resolution of 10 µg. Adsorption equilibria were measured at multiple temperatures over a broad pressure range extending from subatmospheric conditions up to 30 bar, enabling systematic evaluation of the effects of pressure and temperature on CO_2 uptake. The experimental isotherms were analyzed using the dual-site Langmuir model, accompanied by thermodynamic and kinetic analyses to characterize adsorption energetics and uptake behavior. Furthermore, cyclic adsorption–desorption experiments were conducted to evaluate sorbent stability under different regeneration conditions, supported by complementary physicochemical characterization of the material. The principal contribution of this study lies in extending the experimental characterization of LEWATIT VP OC 1065 to substantially higher CO_2 pressures using a high-resolution gravimetric technique, while integrating equilibrium, thermodynamic, kinetic, and cyclic performance assessments within a single investigation. These findings provide additional experimental data for evaluating the sorbent across a broader range of operating conditions and supporting the development and optimization of CO_2 adsorption processes.

2. Materials and Methods

2.1. Chemicals

A research-grade CO_2 gas (Airgas Part #: CD R200), ultra-high purity N_2 gas (Airgas Part #: NI UHP300), and research-grade helium (He) gas (Airgas Part #: HE R300) were provided by Airgas company (Kalamazoo, MI, USA) with 99.999% purity for CO_2 and N_2 and 99.9999% purity for the He. LEWATIT VP OC 1065 (material 740334) was received from LANXESS Deutschland GmbH company (Dormagen, Germany).

The material was kept cooled in the fridge as recommended by the safety data sheet (SDS) provided alongside the received material container. A ~0.2 g sample was loaded into the MSB bucket and activated by heating under vacuum at 120 °C for 6 h in order to release any gases captured from the surroundings and eliminate any moisture in the pores.

2.2. Materials Characterization

The LEWATIT VP OC 1065 material was characterized through different measurements in order to understand the material's physical and chemical properties which is essential to have insight into its behavior. Namely, thermogravimetric analysis (TGA), Fourier transform infrared spectroscopy (FTIR), Brunauer–Emmett–Teller (BET) surface area, and scanning electron microscopy (SEM) measurements were performed. The RUBOTHERM system was bought from Waters GmbH UB TA Instruments (Hullhorst, Germany) with 10 µg resolution. TGA was performed using a Thermogravimetric Analyzer TGA 8000 from PerkinElmer (Shelton, CT, USA) with (+/−160 mg) sensitivity. Also, from PerkinElmer (Shelton, CT, USA), a FT-IR Spectrometer Spectrum 3 was used for the FTIR spectrum measurements before and after CO_2 measurements. BET measurements were performed using a Micromeritics 3Flex Surface Characterization physisorption analyzer (Norcross, GA, USA) which is provided with a VacPrep 061 sample degas system unit connected to a rotary-vane Welch CRVpro2 (Sheboygan, WI, USA) vacuum pump for sample pretreatment. Also, the machine has a Vacuubrand GMBH + CO KG dry vacuum pump (Wertheim, Germany) for evacuating the system. SEM images were collected using a JEOL IT-200 InTouch microscope (Tokyo, Japan) at different magnifications.

2.3. Magnetic Suspension Balance System and High-Pressure Isochoric Gas Adsorption System

The work of CO_2 gas sorption by LEWATIT VP OC 1065 was carried out using the MSB system assembly [ISOSORP SA (400-150, SG)] that has a mass measurement resolution of 10 µg and a mass sample maximum amount of up to 25 g. The reported uncertainty by the manufacturing company is <0.002%. The gas pressure is controlled by a static gas-dosing system (GDS) [Stat-GDS-COLD-MP—9200/40/2-#TI] that works over the pressure range of 0–150 bar.

Also, the system has a rotary-vane vacuum pump Welch CRVpro4 (Sheboygan, WI, USA) for evacuating the system and for the vacuum measurements. The system is equipped with an electrical heater and Julabo Dyneo DD-600F circulator (Seelbach, Germany) for temperature control during measurements, which works within the range of room temperature and up to 400 °C. Figure 1 shows the main parts of the IsoSORP assembly.

The GDS unit's role is to create the required environment for the tested sample. The GDS unit was particularly built to deliver high-pressure pure gas to the intended sample. Figure 1b illustrates the GDS unit. The MSB essential function is to quantify the sample weight change within a controlled-parameter environment. Here, pressure, temperature, and gas composition are the controlled parameters. This control allows high-accuracy quantification of transport and state such as the processes of sorption or diffusion. The measurement results are monitored, recorded, and plotted via the associated software. The MSB comprises a very-high-sensitivity microbalance and a magnetic coupling to connect the sample to the microbalance. The microbalance relates to an electromagnet which raises a permanent magnet at which the sample holder is connected, and consequently the sample weight change is measured. The microbalance is located outside the chamber under ambient atmospheric conditions; thus, a free suspension state is created through the wall of the chamber. Therefore, the physical connection between the balance and the sample is eliminated. An additional suspension state is provided in this setup where a sinker with a predefined volume is lifted as well, allowing the actual surrounding gas density to be determined. The suspension is controlled by a direct analogous control circle (PID controller and position transducer). This control system modifies the voltage amount on the electromagnet in a way that the suspended magnet is held continually in a vertical situation. A microcontroller-driven digital setpoint unit superimposed to the direct PID

unit permits the suspension magnet to be in various positions. Figure 1c shows the MSB unit parts.

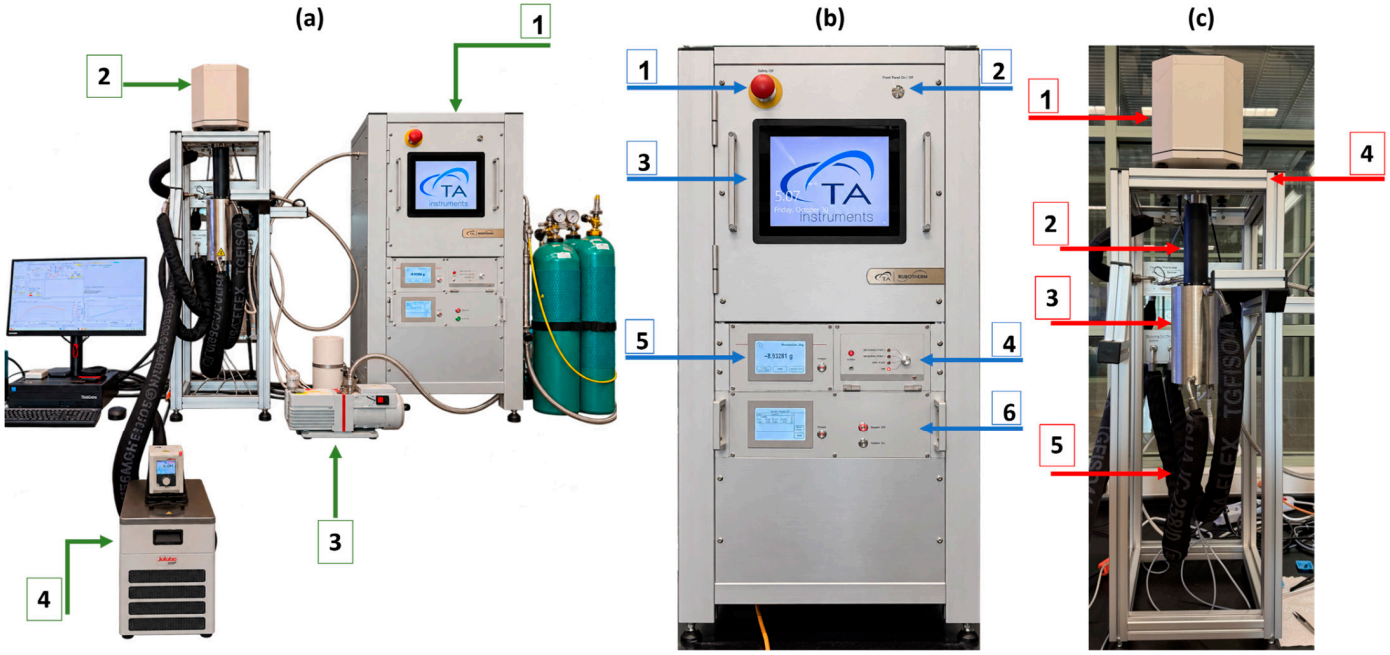


Figure 1. (**a**) IsoSORP assembly overview; 1. GDS unit, 2. MSB unit, 3. vacuum pump, and 4. Julabo DYNEO DD-600F; (**b**) GDS unit parts: 1. safety-off button, 2. on/off switch for panel PC, 3. panel PC, 4. MSB control unit, 5. MSB display, and 6. temperature controller; (**c**) MSB unit parts: 1. balance head with microbalance, 2. magnetic coupling, 3. measuring cell, 4. MSB rack, and 5. tubing to circulator.

The P&I diagram of IsoSORP (400-150,S-G) is provided in Figure S1 in the electronic supporting information (ESI). The CO_2 gas adsorption–desorption was carried out at three isotherms 20, 25, and 30 °C, over the range of pressure of 0 to 1000 mbar with 100 mbar increments. Prior to the adsorption–desorption, a pretreatment was applied for the sample under the conditions of vacuum pressure and heating at 120 °C for 6 h. Desorption and regeneration steps in this work were driven by direct conductive heating of the measuring cell wall through the electrical heater of the MSB, combined with dynamic vacuum, so that the sorbent was regenerated in the absence of oxygen. No convective gas sweep or steam stripping was applied. Cyclability test was performed for the tested material by applying 20 cycles of adsorption–desorption of CO_2 at 20 °C. Some cycles were performed after a thermal pretreatment with applying vacuum pressure and some of them were performed after a vacuum-only pretreatment. To cover a wider area of potential applications of the tested material, it was tested for high-pressure performance at 20 °C and up to 30 bar.

3. Results and Discussions

3.1. Thermophysical Properties

3.1.1. TGA Measurements Analysis

The TGA was performed in this work in order to define the thermal stability and thermal limitations of the material tested within the scope of this research to explore it in a proper way without damaging it, as shown in Figure 2. Here, the sample was tested under heating rate of 5.0 °C/min over the range of 30 to 1000 °C. The TGA curve and its corresponding derivative thermogravimetric (DTG) profile are presented in Figure 2. The thermal behavior can be divided into four mass-loss stages based on the experimental data.

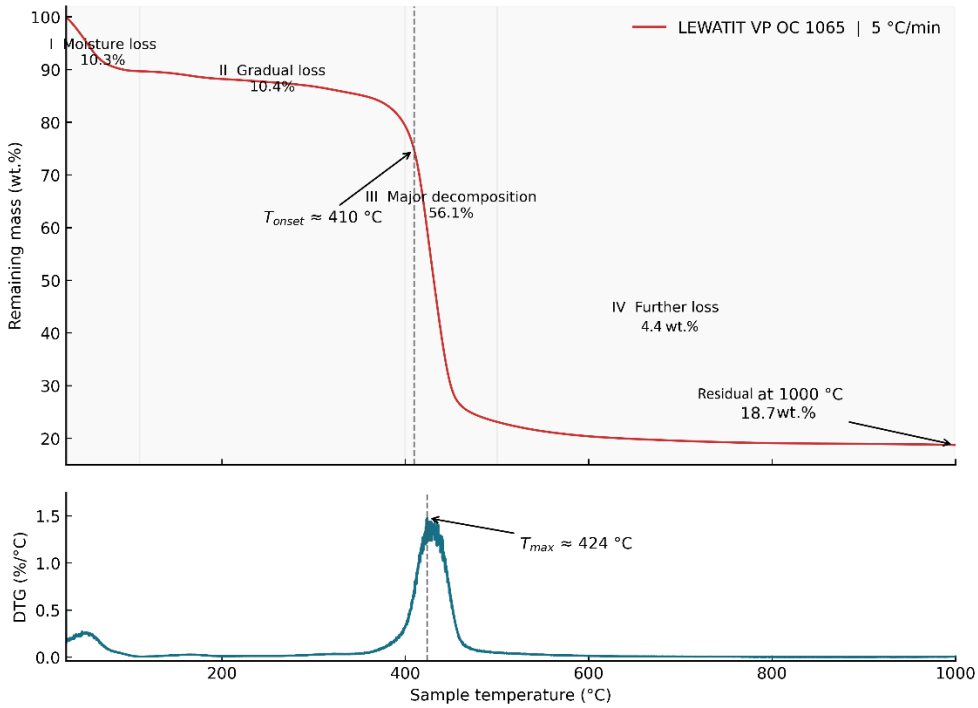


Figure 2. TGA of LEWATIT VP OC 1065 at a heating rate of 5 °C/min, showing four mass-loss stages: (I) moisture desorption (30–110 °C; 10.3%), (II) gradual mass loss (110–400 °C; 10.4%), (III) major thermal decomposition (400–500 °C; 56.1%), and (IV) further mass loss (500–1000 °C; 4.4%). The onset temperature (T_{onset}) of the major decomposition stage was approximately 410 °C, while the maximum degradation rate occurred at approximately 424 °C (T_{max}), as determined from the DTG curve. The final residual mass at 1000 °C was 18.7 wt.%.

The first mass drop stage extend from 30 to 110 °C which is related to the water content of the sample as a physically absorbed moisture. That mass loss was around 10.3% of the sample mass. The second stage, between 110 and 400 °C, showed an additional gradual mass loss of 10.4%. This behavior may involve the release of more strongly retained volatile components and thermally induced changes in the resin's functional groups. However, the precise processes responsible for this stage cannot be conclusively identified from TGA alone.

The third stage, between 400 and 500 °C, represented the principal thermal decomposition event, accounting for a mass loss of ~56.1%. The T_{onset} of this major decomposition stage, determined using the tangent-intersection method, was approximately 410 °C. Determining the onset temperature is essential for establishing the upper thermal boundary of the operating temperature range, as regeneration should be conducted below the temperature at which significant thermal decomposition begins [23]. Derivative thermogravimetric analysis identified the T_{max} at approximately 424 °C. This pronounced decomposition event is attributed primarily to the thermal breakdown of the organic polymeric structure, potentially including degradation of the polystyrene–divinylbenzene backbone and its associated functional groups. The fourth stage, extending from 500 to 1000 °C, accounted for an additional mass loss of ~4.4%, indicating further thermal decomposition of the remaining organic material. The final residual mass at 1000 °C was approximately ~18.7 wt.%.

It is important to emphasize that the onset temperature determined from TGA does not independently establish the maximum safe operating temperature for sorbent regeneration. The thermal stability of amine-functionalized sorbents is also governed by chemical degradation pathways that may occur at considerably lower temperatures, depending on the surrounding atmosphere and exposure duration. For LEWATIT VP OC 1065, Yu

et al. [19] reported that CO_2 adsorption capacity remained stable during 50 h of exposure at 100–150 °C under an inert atmosphere but decreased at 200 °C. They also observed capacity losses of approximately 9% at 120 °C and 23% at 150 °C after 72 h of exposure to concentrated CO_2, attributed to urea formation. Furthermore, oxidative degradation of benzylamine groups became significant above approximately 70 °C in the presence of oxygen, with approximately 30% capacity loss reported after 72 h in air at 80 °C. In contrast, no capacity loss was observed after 48 h of continuous steam exposure, which was attributed to the carbon–carbon anchoring of the amine groups to the polystyrene backbone [19].

Accordingly, the high-temperature decomposition characteristics observed in the present TGA measurements should be distinguished from the chemical stability requirements of repeated adsorption–desorption operation. Based on these considerations, a regeneration temperature of 120 °C under dynamic vacuum conditions was adopted in the present study. This regeneration protocol was selected to facilitate CO_2 desorption while limiting exposure to the more severe thermal conditions associated with polymer decomposition, although its suitability for repeated operation must ultimately be assessed through the cyclic stability measurements.

3.1.2. FTIR Spectrometry

FTIR data of LEWATIT samples were acquired before and after the process of CO_2 adsorption. This investigation was done in order to define the functional groups and the chemical bonds in the samples of LEWATIT. Figure 3 displays the mid-IR region (4000–550 cm^{-1}) data of the LEWATIT before and after the CO_2 capture process.

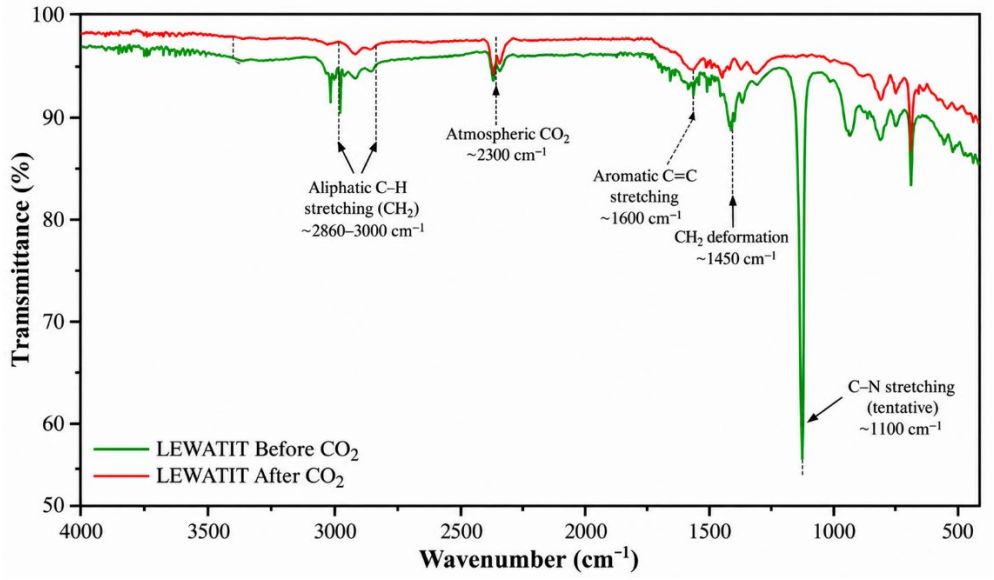


Figure 3. FTIR spectra of LEWATIT VP OC 1065 before and after CO_2 adsorption, showing the characteristic absorption bands of the amine-functionalized polymer. The pronounced reduction in absorption intensity near 1100–1150 cm^{-1} following CO_2 adsorption indicates a substantial adsorption-induced change in the local chemical environment of the resin, potentially involving C–N stretching vibrations associated with its amine functionalities.

The FTIR spectra of fresh and used LEWATIT VP OC 1065 exhibit several characteristic absorption bands associated with the polymeric backbone and amine functional groups. The absorption bands observed between approximately 2860 and 3000 cm^{-1} are attributed primarily to aliphatic C–H stretching vibrations, particularly those associated with methylene (CH_2) groups in the benzylamine functionalities and polymer structure. Differences in the intensity and resolution of these bands between the fresh and used samples may reflect

changes in the local chemical environment or measurement conditions and should not be interpreted as evidence of the loss of specific C–H functional groups.

The features observed near 2300 cm^{-1} are not assigned to C≡C stretching, as alkyne functionalities are not expected in the chemical structure of this resin. Instead, absorption in this region may arise from atmospheric CO_2 contributions to the FTIR background or optical path and is therefore not used to infer changes in the resin structure.

The absorption bands near 1600 cm^{-1} are consistent with aromatic C=C stretching vibrations of the polystyrene–divinylbenzene framework, potentially overlapping with N–H bending vibrations associated with primary amine groups. Bands near 1450 cm^{-1} can be associated with CH_2 deformation and aromatic skeletal vibrations. A particularly sharp and intense absorption band is observed near 1100–1150 cm^{-1} in the fresh resin, which may include contributions from C–N stretching vibrations associated with the amine functionalities. Because multiple vibrational modes can overlap within the fingerprint region, this assignment remains tentative rather than definitive.

Comparison of the FTIR spectra before and after CO_2 adsorption reveals a pronounced reduction in the absorption intensity of the sharp band near 1100–1150 cm^{-1}. Since both samples were analyzed under identical experimental conditions, with CO_2 adsorption being the only difference in their treatment histories, this substantial spectral change can be directly associated with the CO_2 adsorption process. The marked reduction in band intensity suggests that CO_2 adsorption significantly alters the local vibrational environment of the amine-containing polymer structure, consistent with the involvement of amine functional groups in the CO_2 capture mechanism. This observation provides spectroscopic evidence of an adsorption-induced change in the resin's chemical environment and supports the interaction between CO_2 and the amine functionalities. However, because multiple vibrational modes overlap in the fingerprint region, the observed spectral change alone does not conclusively identify the resulting CO_2-bound species, such as ammonium carbamate, carbamic acid, or bicarbonate. Previous computational investigations of this resin have suggested that water-assisted carbamic acid formation may be energetically favorable under certain conditions, whereas bicarbonate formation becomes more relevant in the presence of substantial co-adsorbed water [16,17]. Definitive identification of the adsorbed species would require complementary techniques, such as in situ diffuse reflectance infrared spectroscopy or solid-state ^{13}C NMR.

3.1.3. Brunauer–Emmett–Teller (BET) Surface-Area Analysis

The BET method is a common procedure implemented to compute the surface area based on the N_2 gas adsorption. The N_2 gas adsorption in this analysis is based on the physisorption mechanism. Normally, the data sets are collected over a relative pressure (P/Po) range of 0.05 to 0.3 for such analysis. This model (BET) surface area is estimated from the monolayer adsorption capacity of the adsorbent material.

This estimates the volume of the very first single layer of gas molecules/atoms adsorbed on the material's surface. In this work, the tested sample was degassed in the VacPrep 061 Preparation Station at 80 °C under vacuum environment for 24 h to ensure all the moisture is released out of the sample. The physisorption of N_2 analysis was performed under liquid N_2 cooling medium at 77.95 K. The BET results of N_2 adsorption are shown in Figure 4. The graph shows the quantity adsorbed in terms of (cm^3/g STP) at the specified relative pressure (P/Po) for the sample in three different ports. The tabulated data is provided in Table S1 in the ESI. The multipoint BET surface area retrieved by this measurement for the sample is the 31.05 + 0.93 m^2/g average of the three port values, while the single-point surface area at (P/Po = 0.3) is 30.07 m^2/g in port 1 which is a moderately high surface area. This gives more contact range for mass transfer, which should improve the efficiency of

gas adsorption applications for the material. The actual equipment picture is reported in Figure S2 in the ESI file.

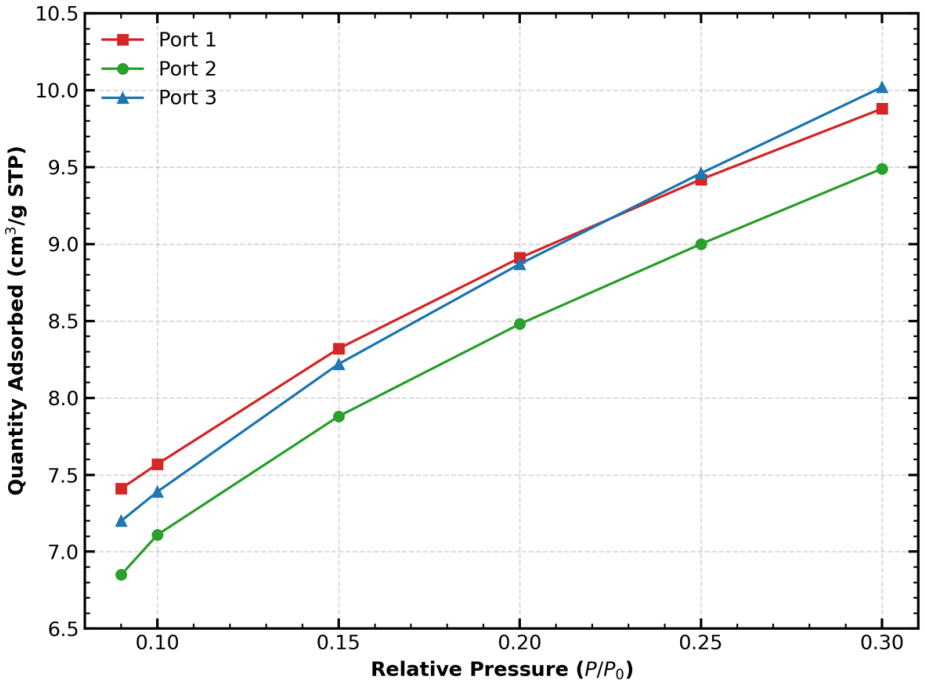


Figure 4. N_2 physisorption isotherms (77 K) for the amine-functionalized resin evaluated within the standard multipoint BET relative pressure range ($P/P° = 0.05–0.30$). The linear uptake profiles across three independent measurement ports yield an average specific surface area of ~31 m^2/g, consistent with macroporous polymeric architectures.

It should be stressed that for an amine-functionalized chemisorbent the BET surface area is not the primary descriptor of the CO_2 capacity: the uptake is governed by the density and accessibility of the amine sites distributed throughout the polymer matrix rather than by the geometric surface available for physisorption. The value measured here (31.05 ± 0.93 m^2/g) is consistent with independent reports for this macroporous resin, which give a surface area of approximately 25 m^2/g, a pore volume of approximately 0.2 cm^3/g, and a mean pore radius of approximately 38 nm [19], as well as a mean pore diameter of approximately 25 nm [20]. The macroporous architecture serves principally as a low-resistance transport network that delivers CO_2 to amine sites within the polymer bulk. Two observations from the present dataset corroborate this picture: the measured capacity of 2.76 mmol/g far exceeds what a surface of this magnitude could accommodate through surface-limited physisorption alone, and the rapid sorption kinetics reported in Section 3.2 show that intraparticle transport through the macropore network is not rate-limiting. The dominant role of chemisorption at amine sites distributed through the polymer phase, rather than surface-area limited adsorption, is well established for this class of materials [16,17].

3.1.4. Scanning Electron Microscopy Analysis

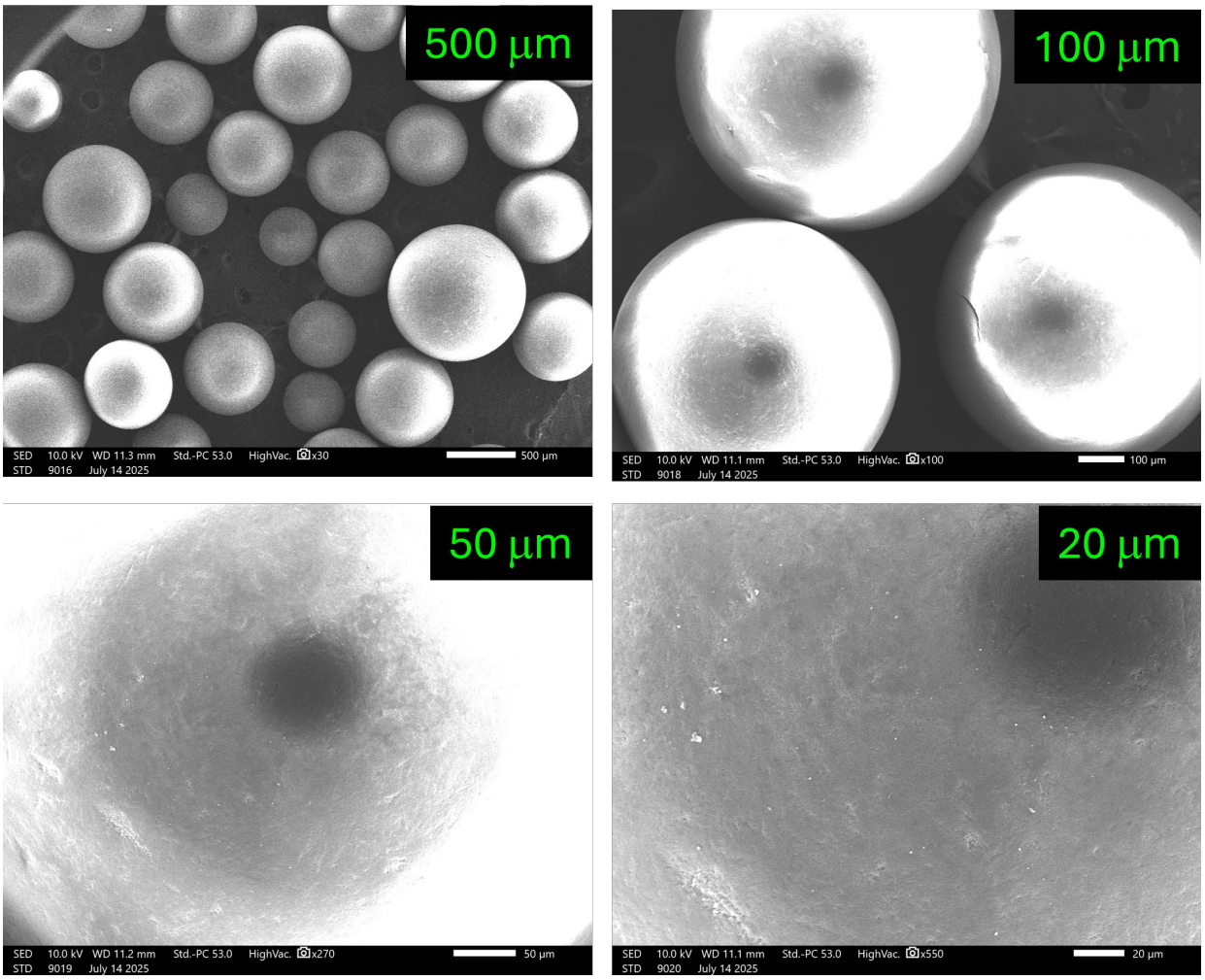
To elucidate the morphological characteristics and elemental distribution of the amine-functionalized resin, SEM images coupled with energy-dispersive X-ray spectroscopy (EDS) was employed. As illustrated in Figure 5, the low-magnification micrographs (500 µm) reveal a highly uniform, spherical bead morphology characterized by a narrow particle-size distribution and a macroscopically smooth exterior. Such structural uniformity is highly advantageous for bulk-scale column or fixed-bed adsorption applications, as it minimizes pressure drop and promotes homogeneous gas-flow distribution. Further examination

at higher magnifications (100 µm to 20 µm) exposes a complex, micro-textured surface topography. This localized surface roughness significantly increases the effective external surface area, thereby facilitating rapid gas–solid interfacial diffusion and enhancing the overall adsorption kinetics required for efficient gas–solid contacting.

Complementary EDS analysis confirms the carbon-rich composition of the functionalized polymer backbone. While the high-density carbon signal dominates the spectrum, the surface N_2 and oxygen functional groups fall near the detection limits of this specific localized scan, underscoring the necessity of the FTIR analysis (Section 3.1.2) to definitively confirm the presence of the amine-active sites.

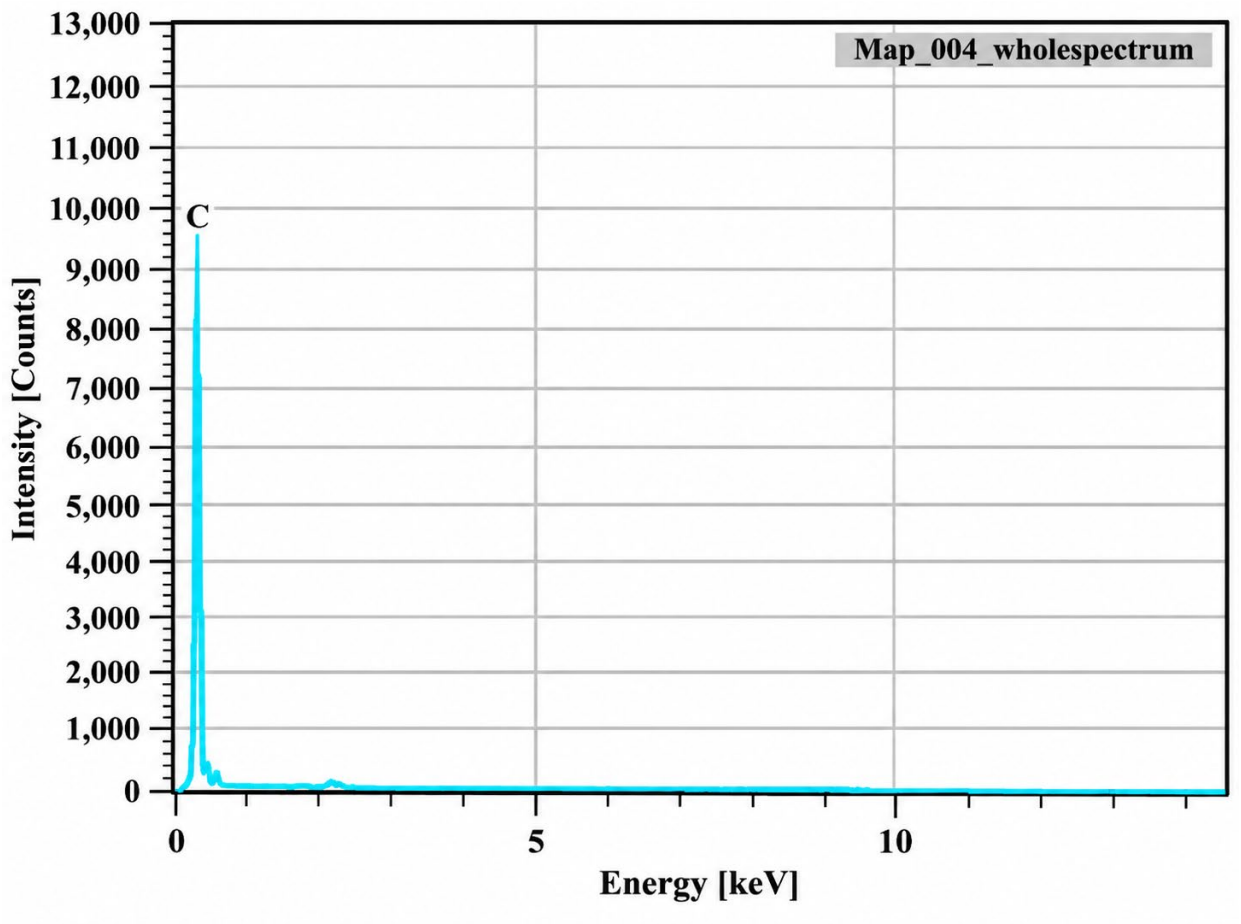
3.2. Low-Pressure CO_2 Sorption Equilibria and Cyclic Stability

The gravimetric excess adsorption of CO_2 was quantified with high precision utilizing an MSB to evaluate the material's viability for sub-atmospheric and low-pressure CO_2 separation applications. Measurements were conducted across three discrete isotherms (20, 25, and 30 °C) within a pressure domain of 0 to 1000 mbar. Both adsorption and desorption pathways were recorded continuously to assess cyclic reversibility and thermodynamic binding affinity.



(**a**)

Figure 5. *Cont.*



(**b**)

Figure 5. (**a**) SEM micrographs of the amine-functionalized macroporous resin at varying magnifications (500 µm, 100 µm, 50 µm, and 20 µm) highlighting the uniform spherical morphology and surface texture. (**b**) Energy-dispersive X-ray spectroscopy (EDS) profile of the amine-functionalized resin. The dominant carbon (Kα at 0.277 keV) peak confirms the primary structure of the polymeric backbone.

These measurements employ pure CO_2 over 100 to 1000 mbar. They describe the sorbent in the concentrated CO_2 regime, and no extrapolation to dilute feeds is attempted in this work. Experimental assessments of this same resin under 400 ppm CO_2 feeds are available in dedicated fixed-bed and breakthrough studies [15,17,21]. The role of the present dataset is complementary to those studies: it establishes, with high resolution and with full adsorption and desorption branches, the equilibrium bounds, the hysteresis behavior, the cyclic stability, and the sorption kinetics of the material across a wide pressure and temperature window measured on a single well-characterized sample.

Figure 6 presents the individual adsorption–desorption isotherms for each of the three operating temperatures. A distinct, macroscopic hysteresis loop is universally observed across all thermal profiles. The divergence between the adsorption (solid lines) and desorption (dashed lines) curves signifies that a substantial fraction of the CO_2 is strongly retained by the material even as the partial pressure is incrementally reduced. This hysteresis is a classical indicator of chemisorption, confirming that the primary amine groups on the polymer backbone form stable chemical complexes such as carbamates or bicarbonates with the CO_2 molecules, effectively preventing premature gas release under standard vacuum conditions. Table 2 benchmarks this performance against the existing literature, revealing that the

evaluated aminated resin exhibits a highly competitive excess CO_2 capacity (~2.76 mmol/g), verifying its substantial potential for broad carbon capture implementations.

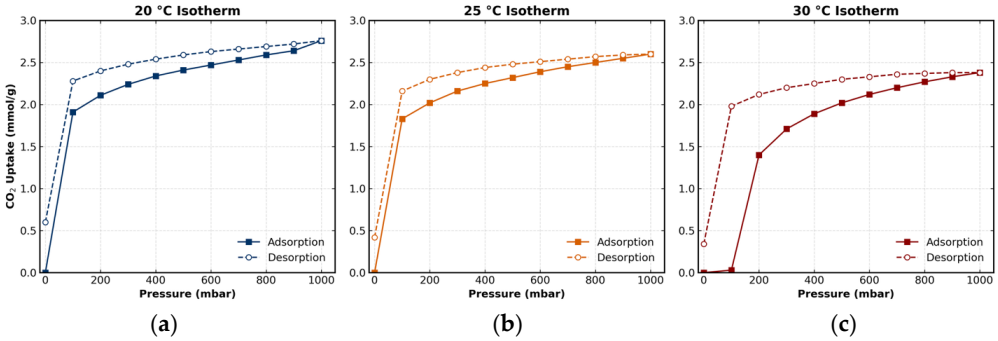


Figure 6. Adsorption and desorption isotherms of CO_2 on the amine-functionalized resin at (**a**) 20, (**b**) 25, and (**c**) 30 °C. The pronounced macroscopic hysteresis universally observed across all temperatures is indicative of strong adsorbate–adsorbent interactions and localized chemisorption. Error bars are not drawn: the manufacturer-specified uncertainty of the MSB is below 0.002% of the reading, and the run-to-run repeatability established over twenty replicate cycles is ±0.016 mmol/g; both are smaller than the plotted symbols.

Table 2. CO_2 adsorption capacity in this work and other materials in the literature.

Material	Capacity and Conditions	Reference
LEWATIT VP OC 1065	2.76 mmol/g at 20 °C, 1000 mbar pure CO_2, dry (MSB, equilibrium)	This Work
LEWATIT VP OC 1065	~2.8 mmol/g at 30 °C, 0.8 bar CO_2 (80 vol%), dry (gravimetric, equilibrium)	[16]
LEWATIT VP OC 1065	2.5 mmol/g at 40 °C, 0.5 bar CO_2, dry	[20]
LEWATIT VP OC 1065	2.15 mmol/g at 40 °C, 0.15 bar CO_2 (15 vol%), dry (fixed bed, dynamic)	[19]
LEWATIT VP OC 1065	~1.6 mmol/g at 20 °C, 910 mbar pure CO_2 (fixed bed, dynamic)	[15]
LEWATIT VP OC 1065	~1.1 mmol/g at 20 °C, 0.4 mbar CO_2 (400 ppm)	[17]
Zeolite 13X	~4.5 mmol/g at 25 °C, ~1 bar pure CO_2, dry (volumetric, equilibrium)	[24]
Activated carbon (Norit RB2)	~2.6 mmol/g at 25 °C, ~1 bar pure CO_2, dry (gravimetric, equilibrium)	[25]
HKUST-1 (Cu-BTC)	~4.2 mmol/g at 25 °C, 1 bar pure CO_2, dry (gravimetric, equilibrium)	[25]
Mg-MOF-74	8.0 mmol/g at 23 °C, 1 bar pure CO_2, dry (equilibrium)	[26]
PEI impregnated MCM-41 (50 wt% PEI)	~2.5 mmol/g at 75 °C, 1 atm pure CO_2, dry (TGA, flow)	[27]
Triamine grafted pore expanded MCM-41	~2.6 mmol/g at 25 °C, ~1 bar pure CO_2, dry (gravimetric, equilibrium)	[28]

Direct comparison of uptake values across studies requires careful matching of temperature, CO_2 partial pressure, humidity, and measurement mode, because each of these variables changes the observed capacity of a strongly exothermic chemisorbent considerably. For the same commercial resin, the present equilibrium value of 2.76 mmol/g at 20 °C and 1000 mbar is in close agreement with the approximately 2.8 mol/kg measured gravimetrically at 303 K under 0.8 bar CO_2 partial pressure by Veneman et al. [16]. Values reported at higher temperatures or lower partial pressures are necessarily lower: 2.5 mol/kg at 40 °C and 0.5 bar [20] and 2.15 mol/kg at 40 °C and 0.15 bar [19]. Dynamic fixed-bed measurements yield lower working capacities than static equilibrium measurements at nominally similar conditions, as illustrated by the approximately 1.6 mmol/g at 20 °C and 910 mbar reported by Bos et al. [15], and dilute feeds reduce the capacity further, to approximately 1.1 mol/kg at 400 ppm and 20 °C [17]. Within this context, the values measured in this work on a rigorously dried sample with full buoyancy correction (Figure S3 shows the buoyancy results) are consistent with the established literature range for this material. The

benchmark sorbents in Table 1 are listed at matched conditions of about 1 bar pure CO_2 and near-ambient temperature, except the PEI impregnated silica, which reaches its maximum capacity at 75 °C [27]. On this basis, the resin lies between activated carbon and zeolite 13X in capacity and is close to the amine-grafted silica, while it retains the high heat of adsorption and selectivity of a chemisorbent.

To better contextualize the temperature dependency of the uptake capacity, the unified adsorption profiles and their maximum equilibrium values at 1000 mbar are compared in Figure 7. Consistent with the highly exothermic nature of amine–CO_2 chemisorption, the total CO_2 capacity demonstrates an inverse relationship with temperature. The sorbent achieved its highest adsorption magnitude of 2.76 mmol/g at 20 °C and 1000 mbar. While the capacities at 20 °C and 25 °C remain tightly clustered, a more pronounced reduction in capture efficiency is observed at 30 °C, as the elevated thermal energy begins to overcome the enthalpy of adsorption.

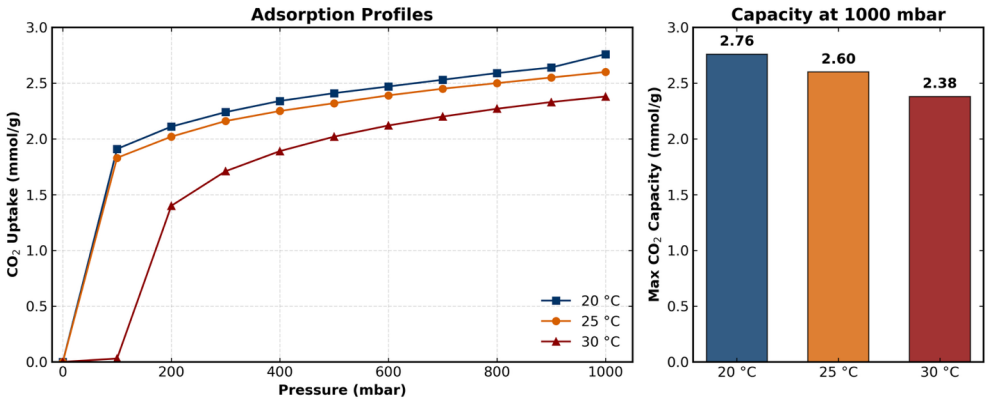


Figure 7. (**a**) Overlay of pure CO_2 adsorption profiles across the evaluated temperature range. (**b**) Maximum equilibrium CO_2 uptake capacities at 1000 mbar, highlighting optimal capture performance at the 20 °C isotherm.

One data quality limitation must be acknowledged. The first point of the 30 °C adsorption branch (0.02 mmol/g at 99 mbar) was excluded from the isosteric heat analysis due to evidence of incomplete equilibration. Examination of the corresponding raw mass-versus-time profile revealed a sustained increase in the corrected mass signal without reaching a clear plateau, despite the pressure remaining approximately constant at 100 mbar. Furthermore, the recorded temperature increased from approximately 30 to 32 °C during this measurement, indicating additional thermal instability. Although the instrument's predefined short-term stability criterion was satisfied, the combined mass and temperature profiles indicate that the recorded uptake was not representative of adsorption equilibrium at the nominal experimental temperature. Three observations establish this conclusively. First, the value is two orders of magnitude below the uptakes measured at the same pressure at 20 °C (1.90 mmol/g) and 25 °C (1.82 mmol/g), and no physically admissible temperature dependence can produce such a collapse over a 5 K increment, since it would imply an isosteric heat of several hundred kJ/mol, far outside the range established for this material [16,20]. Second, the desorption branch of the same isotherm passes through 1.99 mmol/g at 100 mbar, and a two-orders-of-magnitude gap between the adsorption and desorption branches at identical conditions on the same sample is possible only if the adsorption point had not reached equilibrium. Third, all remaining points of the 30 °C branch are smoothly consistent with the 20 and 25 °C isotherms. This point is therefore retained in Figure 6 for transparency but is excluded from the isosteric heat analysis presented later in this section.

The low-pressure part of the isotherm sets the working capacity of a vacuum swing process and the residual loading after regeneration. Figure 8 illustrates the adsorption equilibria on a semi-logarithmic scale, visually expanding the sub-atmospheric capture regime. The exceptionally steep initial slope of these isotherms confirms that the amine-active sites possess a high thermodynamic affinity for CO_2, rapidly sequestering the gas well before bulk pore-filling mechanisms initiate.

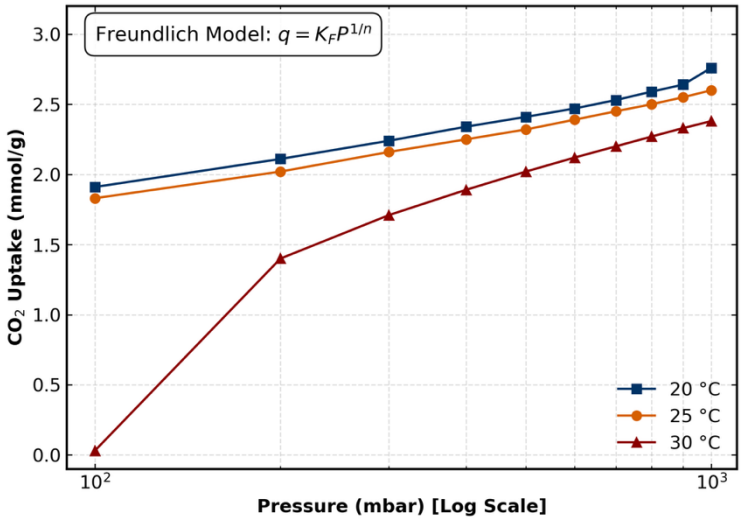


Figure 8. Semi-logarithmic representation of the low-pressure CO_2 adsorption equilibria (≥100 mbar). This scaling highlights the steep sub-atmospheric capture performance characteristic of high-affinity binding sites, demonstrating the applicability of the Freundlich empirical model ($q = K_F P^{1/n}$) for heterogeneous surface interactions.

To quantify this behavior, the data distribution was evaluated against the principles of the empirical Freundlich model ($q = K_F P^{1/n}$). Linearization of the adsorption data ($\ln q$ vs. $\ln P$) yielded robust fits across the evaluated pressure regime ($R^2 > 0.98$). At the optimal capture temperature of 20 °C, the material exhibited a high-capacity factor ($K_F = 0.92$) and an adsorption intensity factor of $1/n = 0.160$. In Freundlich kinetics, a $1/n$ value significantly lower than 1.0 can be considered as a potential indication of chemisorption. This confirms that the surface interactions are highly heterogeneous, a condition strictly characteristic of a functionalized polymer resin containing a broad energetic distribution of accessible primary and secondary amine-binding sites. Furthermore, the model parameters accurately reflect the thermodynamic temperature limitations observed in the bulk capacity. As the temperature increased to 30 °C, the capacity factor dropped sharply ($K_F = 0.25$), and the intensity factor increased ($1/n = 0.329$). This shift quantitatively maps the onset of thermal decay, indicating that the elevated thermal energy at 30 °C begins to overcome the chemisorptive bond enthalpies, rendering the active sites less favorable for CO_2 retention.

The Freundlich model is empirical and does not give a saturation capacity. To provide parameters that are suitable for process simulation, the absolute adsorption branches at 20, 25, and 30 °C were also fitted with a dual-site Langmuir (DSL) model, $q = q_1 b_1 P/(1 + b_1 P) + q_2 b_2 P/(1 + b_2 P)$, where q_1 and q_2 are the saturation capacities of the strong and weak sites and b_1 and b_2 are the corresponding affinity constants. The site capacities were shared between the three temperatures, and the affinity constants were fitted for each temperature. The first point of the 30 °C isotherm was excluded for the reason given above. Figure 9 compares the model with the measured data, and Table 3 lists the parameters (T, b_1, b_2, regression R^2, root mean square error (RMSE) quantifying the average magnitude

of deviations between experimental and predicted CO_2 adsorption capacities, average absolute relative deviation (AARD) expressing the average absolute percentage difference between experimental and predicted adsorption capacities). The model describes all three isotherms with $R^2 \geq 0.997$ and an average absolute relative deviation below 0.8%. The strong site capacity of 1.87 mmol/g is close to the uptake measured at 100 mbar and 20 °C (1.90 mmol/g). This shows that the strong sites are almost saturated at the lowest pressure of this study, and that the uptake between 100 and 1000 mbar is carried by the weak sites. The result agrees with the decrease in the isosteric heat from 102 to 49 kJ/mol with loading that is reported later in this section. The strong site affinity constant decreases with temperature, as expected for an exothermic process. The 30 °C parameters carry a larger uncertainty, because the low-pressure part of that branch deviates from the trend of the 20 and 25 °C isotherms, as noted above for its first point.

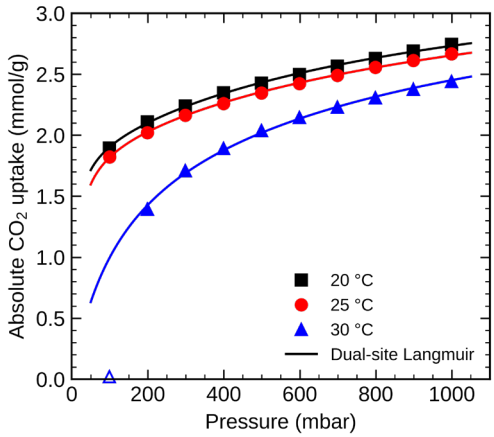


Figure 9. Absolute CO_2 adsorption isotherms at 20, 25, and 30 °C (symbols) and dual-site Langmuir fits with shared site capacities (lines). The open symbol is the first point of the 30 °C branch, which was excluded from the fit.

Table 3. Dual-site Langmuir parameters for the absolute CO_2 adsorption isotherms. The site capacities $q_1 = 1.87$ mmol/g and $q_2 = 1.70$ mmol/g are shared between the three temperatures.

T (°C)	b_1 (bar^{-1})	b_2 (bar^{-1})	R^2	RMSE (mmol/g)	AARD (%)
20	135.7	1.063	0.9991	0.008	0.30
25	88.4	0.899	0.9992	0.007	0.27
30	8.6	0.838	0.9975	0.016	0.78

Although the DSL model provides a satisfactory representation of the experimental adsorption isotherms, the fitted affinity parameter b_1 exhibits a pronounced decrease at 30 °C compared with those obtained at 20 and 25 °C. This behavior should be interpreted with caution, as individual affinity parameters in a multisite adsorption model may be sensitive to parameter correlations and the limited availability of low-pressure measurements. Consequently, the temperature dependence of b_1 alone should not be regarded as a reliable quantitative measure of the adsorption enthalpy. Instead, the isosteric heat of adsorption was evaluated separately using the experimentally measured absolute adsorption isotherms and the Clausius–Clapeyron relation, as discussed in the following section.

To explicitly isolate and quantify the chemisorptive strength of the material, the isothermal hysteresis penalty (Δq) was plotted as a function of pressure in Figure 10. In this context, Δq represents the firmly "retained" or "trapped" CO_2 fraction ($\Delta q = q_{des} - q_{ads}$) at any given pressure increment. The material exhibits a sharp retention penalty at lower pressures, which subsequently flattens and stabilizes as the system approaches 1000 mbar.

This thermodynamic profile effectively maps the dual-mechanism behavior of the sorbent: at low partial pressures, the finite number of amine-active sites are rapidly saturated via strong chemical bonding (yielding high retention), whereas at elevated pressures, the primary mechanism transitions toward standard physisorption within the macroporous voids, allowing the excess bulk gas to be desorbed more readily without an associated chemical energy penalty.

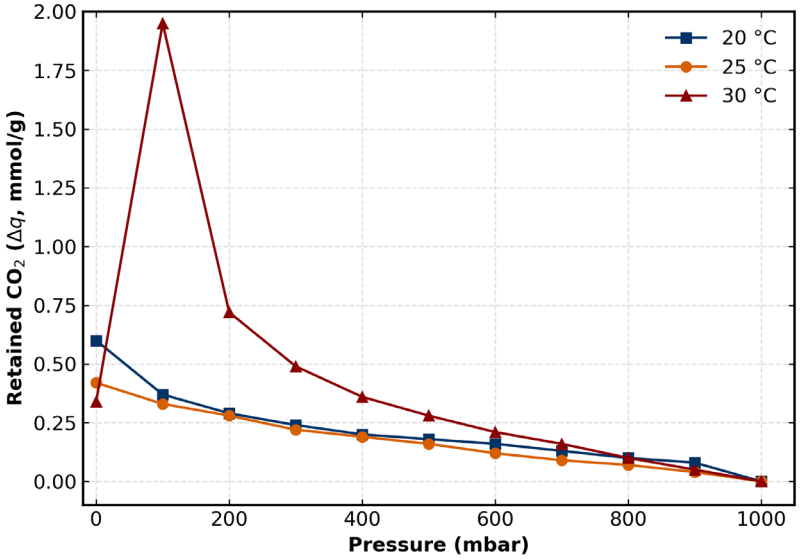


Figure 10. Pressure-dependent isothermal hysteresis penalty (Δq), quantifying the fraction of strongly retained CO_2 relative to the total uptake. This explicitly maps the transition boundary between the chemisorption (high retention) and physisorption (low retention) regimes.

Figure 11 shows the maximum CO_2 adsorption capacity of each cycle of the 20 cycles at 20 °C and 1000 mbar. The red bars are the cycles with heating activation which show no real decline in the adsorption capacity of CO_2. The value of adsorption in these cycles ranged from 2.71 to 2.76 mmol/g. The sample exhibits a decline in the excess CO_2 adsorption capacity without using heat in the regeneration stage showing the maximum adsorption values 1.94 to 2.24 mmol/g. Considering the adsorption capacities obtained under each regeneration condition at 20 °C and 1000 mbar, the twelve thermally regenerated cycles yielded a mean of 2.727 ± 0.016 mmol/g, corresponding to a relative standard deviation of 0.59%, indicating excellent cycle-to-cycle consistency. The eight vacuum-only cycles give 2.07 ± 0.11 mmol/g, corresponding to a 24% reduction in the working capacity relative to thermal-vacuum regeneration.

However, this reduction does not necessarily indicate irreversible deterioration of the adsorbent. As demonstrated in Figure 11a, the adsorption capacity was restored to 2.73 mmol/g in Cycle 18 following thermal activation, corresponding to approximately 98.9% of the initial adsorption capacity (2.76 mmol/g). Furthermore, following the completion of all 20 adsorption–desorption cycles and subsequent thermal activation, the material exhibited an excess CO_2 adsorption capacity of approximately 2.58 mmol/g at 1 bar during the high-pressure adsorption measurements (detailed in Section 3.3), corresponding to approximately 93.5% of the initial capacity. The slight difference may be associated with the different pressure dosing procedures, as the pressure was increased stepwise during the cyclic measurements, whereas it was raised directly to 1 bar during the subsequent high-pressure measurements. These findings suggest that the reduced adsorption capacities observed during vacuum-only regeneration were primarily associated with incomplete regeneration rather than irreversible material degradation. Overall, the material maintained

most of its original adsorption capacity despite repeated adsorption–desorption and thermal activation processes, demonstrating good cyclic stability. Figure S4 reveals the 20 cycles of adsorption–desorption measurement of the tested material.

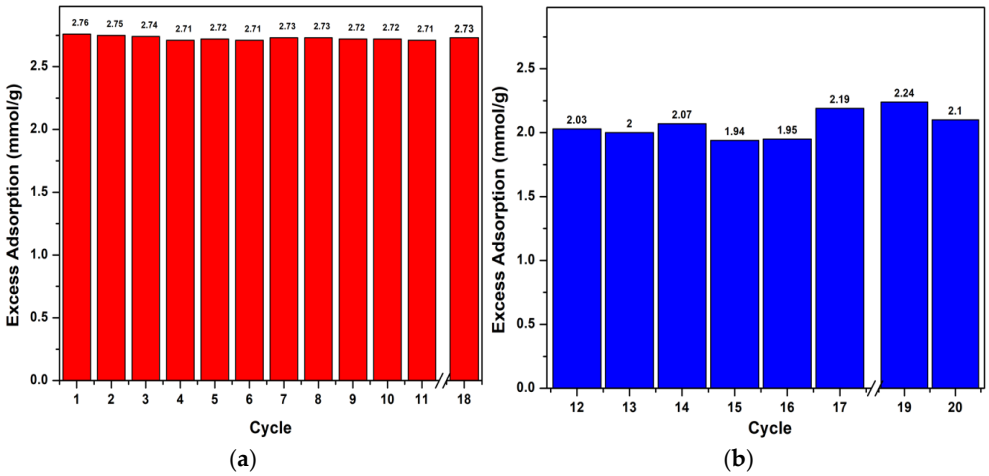


Figure 11. Maximum capacity of CO_2 adsorption cycles at 20 °C and 1000 mbar: (**a**) hot activation and (**b**) cold activation. These results revealed that both physisorption and chemisorption are involved. Here, the decline in the adsorption capacity within the cycles that were activated by pulling vacuum only means the sample either needs more time under vacuum or needs heating to release the held gas.

To inform the design and optimization of future continuous-capture processes, the transient adsorption and desorption kinetics of the amine-functionalized resin were evaluated. Figure 12 presents the time-resolved CO_2 uptake and release profiles for two distinct activation strategies: vacuum-only regeneration (Cycle 17) and thermal-vacuum regeneration at 120 °C (Cycle 18).

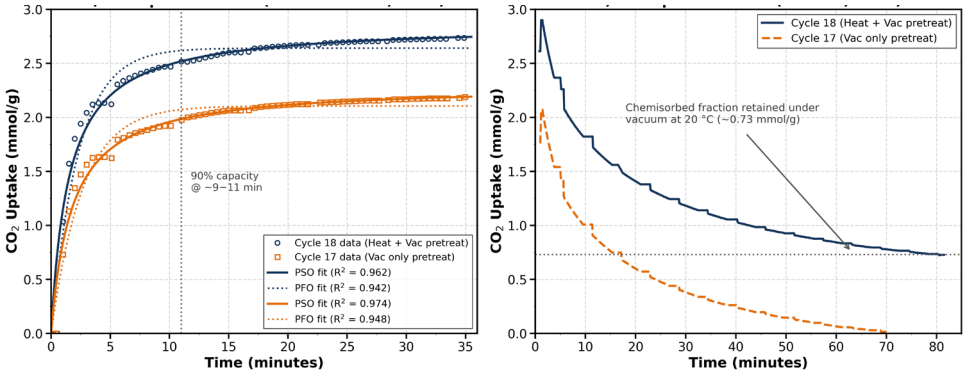


Figure 12. Transient CO_2 sorption kinetics at 20 °C. (**a**) Adsorption from vacuum to 1000 mbar for Cycle 18 (thermal-vacuum pretreatment) and Cycle 17 (vacuum-only pretreatment): measured data (symbols) together with pseudo-second-order (solid lines) and pseudo-first-order (dotted lines) fits; both cycles reach 90% of their equilibrium capacity within 9 to 11 min. (**b**) Desorption under dynamic vacuum at 20 °C: Cycle 17 releases its complete working capacity, whereas Cycle 18 retains approximately 0.73 mmol/g, corresponding to the chemisorbed fraction that requires thermal energy for release.

As illustrated in Figure 12a, the adsorption kinetics exhibit a rapid initial uptake, with both cycles reaching 90% of their respective equilibrium capacities within 9 to 11 min. To place this observation on a quantitative footing, the transient uptake data were fitted with the pseudo-first-order model, $q(t) = q_e(1 - \exp(-k_1 t))$, and the pseudo-second-order

model, $q(t) = q_e^2 k_2 t/(1 + q_e k_2 t)$. For Cycle 17 the fits give $k_1 = 0.378$ min^{-1} ($R^2 = 0.948$) and $k_2 = 0.250$ g mmol^{-1} min^{-1} ($R^2 = 0.974$), and for Cycle 18 they give $k_1 = 0.434$ min^{-1} ($R^2 = 0.942$) and $k_2 = 0.234$ g mmol^{-1} min^{-1} ($R^2 = 0.962$). The pseudo-second-order model describes both datasets better, a behavior commonly associated with uptake controlled by chemical interaction with the surface rather than by intraparticle diffusion, which is consistent with the chemisorption-dominated mechanism established by the hysteresis and isosteric heat analyses. It should be noted that the gas-dosing system requires 10 to 12 min to raise the pressure from vacuum to 1000 mbar and that the sample uptake closely tracks the pressure ramp during this period; the fitted rate constants are therefore effective values under the applied dosing protocol, and the intrinsic sorption kinetics of the material are at least as fast as these values indicate. In either reading, gas-phase delivery rather than intraparticle diffusion limits the observed uptake rate, confirming that the macroporous architecture of the resin poses no kinetic barrier at these conditions.

The desorption branches in Figure 12b quantify the regeneration behavior directly. Under dynamic vacuum at 20 °C, the Cycle 17 sample, whose chemisorption sites were still occupied from the preceding cycles because it had been regenerated by vacuum only, releases essentially its complete working capacity, with a residual of only 0.02 mmol/g after 70 min. In contrast, the Cycle 18 sample, which entered the measurement fully regenerated after thermal treatment at 120 °C and therefore adsorbed CO_2 onto its chemisorption sites during the uptake step, retains 0.73 mmol/g under vacuum at 20 °C. Vacuum alone at ambient temperature is thus sufficient to remove the physisorbed fraction but provides insufficient energy to decompose the chemisorbed amine–CO_2 complexes, and thermal input during regeneration is required to restore the full capacity. This retained fraction of 0.73 mmol/g agrees quantitatively with the residual amount observed at zero pressure after the high-pressure desorption cycle in Section 3.3, providing an independent and self-consistent measurement of the strongly bound chemisorbed fraction of this material.

Moreover, the isosteric heat of adsorption (Q_{st}) was determined from the three measured isotherms using the Clausius–Clapeyron relation in its isosteric form, $(\partial \ln P/\partial(1/T))_q = -Q_{st}/R$, where P is the equilibrium pressure, T is the absolute temperature, and R is the universal gas constant. The absolute adsorption branches at 20, 25, and 30 °C were interpolated to fixed loadings across the loading window common to the three isotherms (1.90 to 2.44 mmol/g), and Q_{st} was obtained at each loading from linear regression of ln P against 1/T, with coefficients of determination between 0.88 and 0.94. The first point of the 30 °C isotherm (99 mbar) was excluded from this analysis for the reasons detailed above. Figure 13 shows the result: Q_{st} decreases monotonically from 102.5 kJ/mol at a loading of 1.90 mmol/g to 48.9 kJ/mol at 2.44 mmol/g. The magnitude at low loading is characteristic of chemisorption on amine sites and brackets the values reported independently for this same resin, 75 to 87 kJ/mol by Veneman et al. [16] and approximately 76 kJ/mol by Sonnleitner et al. [20], while the monotonic decrease toward the physisorption range of 20 to 50 kJ/mol [29] as the loading approaches saturation provides direct thermodynamic evidence of the transition from chemisorption-dominated uptake at the finite amine sites toward weaker, physisorption-like binding at higher coverages. Given that only three temperatures spanning 10 K are available, the absolute values carry a meaningful uncertainty, and they should be read as consistent with, rather than a refinement of, the published calorimetric range for this material.

3.3. High-Pressure Experimental Data of CO_2 Capture

To cover all the aspects of the CO_2 gas capture picture in this research. High-pressure data of CO_2 adsorption was collected at 20 °C isotherm and over the pressure range of 0 to 30 bar. The full cycle of adsorption–desorption of the gas by the solid material was

studied at the same pressure points in both of the stages. Within the measurement, 1 bar measuring point was included to match the high- and low-pressure measurements. Figure 14 demonstrates the high-pressure data of the adsorption–desorption cycle of CO_2 gas. The material achieved highest value of adsorption at 30 bar pressure which is 4.65 mmol/g. The hysteresis appearance in the results agrees with the gap which appeared at the low-pressure measurements. The results showed the potential of the material to adsorb more gas at higher pressure. The held amount of gas at zero pressure after the desorption was 0.73 mmol/g which is similar to that one in the low-pressure cyclability experiments. This confirms that both the chemisorption and physisorption are taking place and the active sites of chemisorption have a fixed number so they will be filled and then the material continues to adsorb the gas physically. At the 0.95 bar point, the adsorption value was 2.57 mmol/g compared to 2.66 mmol/g at 999 mbar in the very first experiment of the low-pressure work. These results show the potential of this material for different gas capture applications at high-pressure point sources.

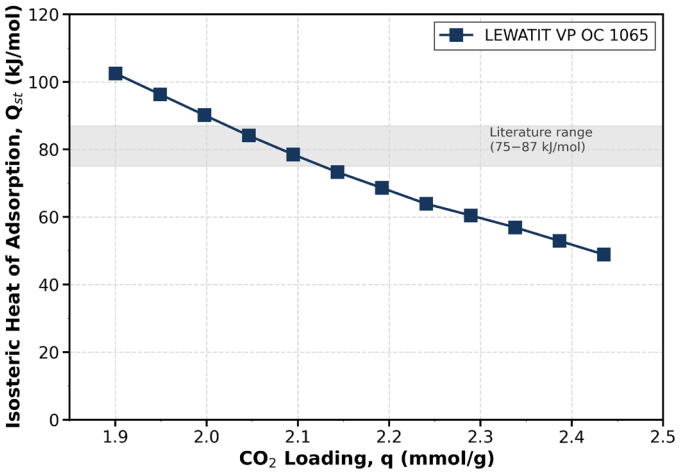


Figure 13. Isosteric heat of adsorption (Q_{st}) of CO_2 on LEWATIT VP OC 1065 as a function of loading, obtained from the 20, 25, and 30 °C absolute adsorption isotherms via the Clausius–Clapeyron relation applied at constant loading. The shaded band indicates the range of isosteric heats reported for this resin in independent studies (75 to 87 kJ/mol) [16,20].

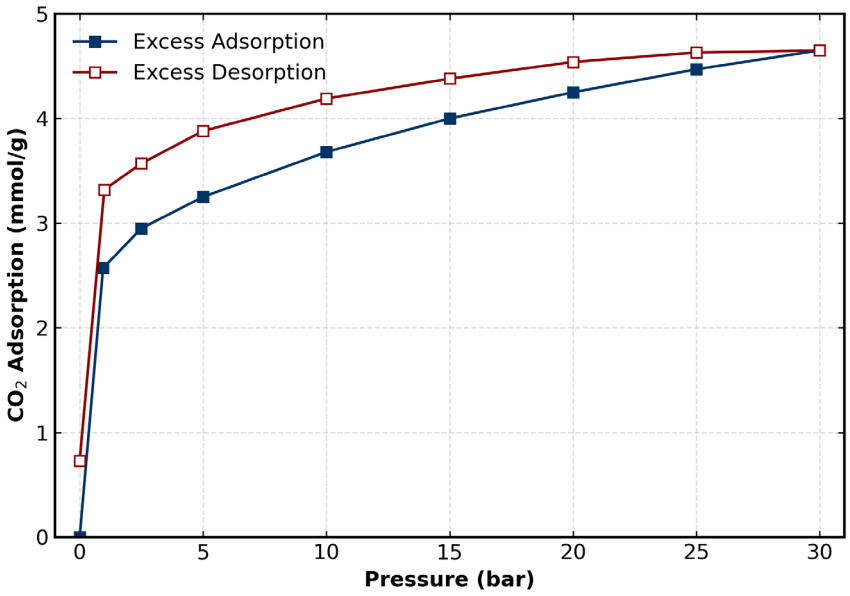


Figure 14. High-pressure measurements of CO_2 adsorption–desorption cycle.

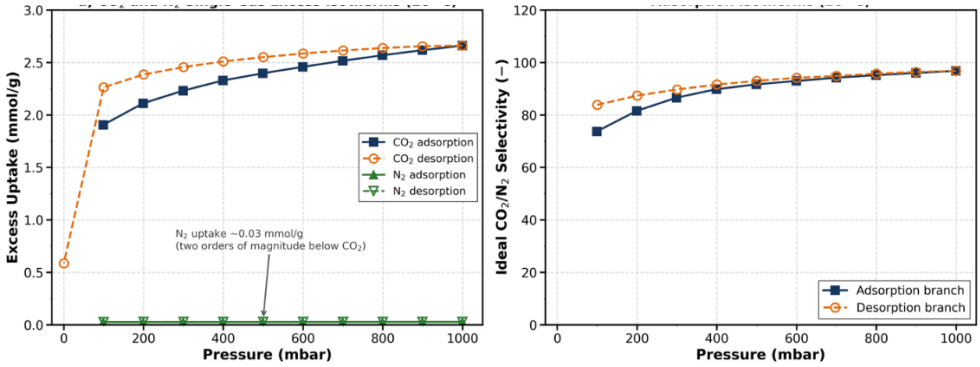
Table 4 summarizes the working capacities that follow directly from the measured isotherms. For a pressure swing from 1000 to 100 mbar, the adsorption branches give 0.85 and 0.84 mmol/g at 20 and 25 °C, and the desorption branches give 0.50, 0.52, and 0.45 mmol/g at 20, 25, and 30 °C. The difference between the two branches is the hysteresis discussed in Section 3.2. The desorption branch value is the conservative estimate for a vacuum swing process. A temperature swing from 20 to 30 °C at 1000 mbar gives 0.30 mmol/g, and a combined swing from 1000 mbar at 20 °C to 100 mbar at 30 °C gives 0.75 mmol/g. The high-pressure data give 2.08 mmol/g on the adsorption branch and 1.33 mmol/g on the desorption branch for a swing from 30 to 1 bar at 20 °C, and 0.97 and 0.45 mmol/g for a swing from 30 to 10 bar. These values come from measurements on a dry sample and do not include bed-scale effects. They give the equilibrium limits that a process model for this material must respect.

Table 4. Working capacities obtained from the measured isotherms. Low-pressure values are from the absolute isotherms, and high-pressure values are from the excess isotherms. The end points of each swing are the measured pressure points closest to the nominal values.

Swing	Branch	Working Capacity (mmol/g)
1000 to 100 mbar, 20 °C	adsorption	0.85
1000 to 100 mbar, 20 °C	desorption	0.50
1000 to 100 mbar, 25 °C	adsorption	0.84
1000 to 100 mbar, 25 °C	desorption	0.52
1000 to 100 mbar, 30 °C	desorption	0.45
20 to 30 °C at 1000 mbar	adsorption	0.30
1000 mbar at 20 °C to 100 mbar at 30 °C	desorption	0.75
29.9 to 0.95 bar, 20 °C	adsorption	2.08
29.9 to 1.17 bar, 20 °C	desorption	1.33
29.9 to 10 bar, 20 °C	adsorption	0.97
29.9 to 10 bar, 20 °C	desorption	0.45

3.4. Selectivity of CO_2 over N_2

Because flue gas and most point source streams consist predominantly of N_2, the selectivity of the sorbent for CO_2 over N_2 is a first-order performance descriptor. To quantify it, an N_2 adsorption and desorption experiment was performed with the MSB at 20 °C over the same 100 to 1000 mbar pressure window used for the CO_2 measurements, and the CO_2 to N_2 selectivity was evaluated as the ratio of the measured excess uptakes at equal pressure and temperature. Figure 15 compares the excess CO_2 isotherm at 20 °C with the resulting selectivity. The selectivity increases from approximately 74 at 99 mbar to approximately 97 at 1000 mbar along the adsorption branch and remains above 84 along the desorption branch, which means that the N_2 uptake stays roughly two orders of magnitude below the CO_2 uptake across the entire window. This behavior is the direct consequence of the capture mechanism: N_2 has no chemical affinity for the amine sites and interacts with the resin only through weak physisorption on a modest surface area, whereas CO_2 is bound chemically at the benzylamine groups. For process purposes, the balance N_2 of a flue gas or other N_2-rich feed therefore does not compete measurably for capacity, and the practically consequential co-adsorbates remain O_2, through the oxidative degradation pathways discussed in Section 3.1.1, and H_2O, through the co-adsorption effects discussed in Section 3.5.



(**a**) (**b**)

Figure 15. CO_2 over N_2 selectivity of LEWATIT VP OC 1065 at 20 °C. (**a**) Excess CO_2 and N_2 adsorption and desorption isotherms at 20 °C. (**b**) CO_2 to N_2 selectivity, evaluated as the ratio of the measured CO_2 and N_2 excess uptakes at equal pressure, along the adsorption and desorption branches. The selectivity ranges from approximately 74 to 97, indicating that the N_2 uptake remains roughly two orders of magnitude below the CO_2 uptake across the entire pressure window.

3.5. Limitations and Outlook

Several limitations of the present study delineate the boundary between sorbent-level screening and process-level demonstration. First, all sorption measurements were performed with pure, dry CO_2, whereas real feed streams additionally contain O_2, N_2, and variable humidity. For this specific resin, co-adsorbed water has been shown to enhance rather than suppress CO_2 uptake, since water enables bicarbonate-forming stoichiometry with a theoretical limit of one mole of CO_2 per mole of amine, compared to one half for the dry carbamate route [16,21]. The dry condition capacities reported here are therefore conservative in this respect. Second, gravimetric MSB measurements quantify equilibrium uptake and intrinsic kinetics on small samples that are free of bed-scale dispersion, heat effects, and pressure drop, and they therefore do not by themselves establish contactor performance. Fixed-bed breakthrough experiments under realistic feed compositions and humidity, together with oxidative aging protocols and post-cycling spectroscopic analysis of amine integrity, are outside the scope of this work. Third, desorption in this work was driven by conductive heating of the measuring cell under dynamic vacuum; steam-assisted and hot gas-sweep regeneration impose different thermal and chemical environments, notably oxygen exposure in air sweeps, which amine-functionalized materials are sensitive to at elevated temperatures [19], and these regeneration modes require dedicated evaluation. Finally, the selectivity measurements in Section 3.4 indicate that the balance N_2 of a flue gas feed does not compete measurably for capacity, so the practically consequential co-adsorbates for future humid feed evaluation are O_2 and H_2O.

4. Conclusions

This work gives an inclusive experimental exploration of an aminated material in terms of characteristics such as the thermal stability of the material, the functional groups and bonding within the material, the material's surface area, and the topography imaging of the material surface. This work explored experimentally the aminated material for sub-atmospheric and high-pressure CO_2 capture and separation. That was carried out through adsorption–desorption tests for the material at three isotherms (20, 25, and 30 °C) and pressure ranges of 0 to 1000 mbar and 0 to 30 bar, to cover a wide range of process conditions. The material showed a high potential for capturing CO_2 with a magnitude of 2.76 mmol/g which is comparable to literature values, and also showed high adsorption capacity of 4.65 mmol/g at 30 bar. The work presented here evaluated the capability of the material to be

utilized multiple times by conducting a cyclability test involving 20 adsorption–desorption cycles using the same sample. The material demonstrated good cyclic stability, recovering approximately 98.9% of its initial CO_2 adsorption capacity following thermal regeneration in Cycle 18. Furthermore, after completing all 20 cycles and subsequent thermal activation, the material retained approximately 93.5% of its initial adsorption capacity, indicating no substantial irreversible deterioration in adsorption performance. Moreover, the kinetics of the capture process was assessed. The kinetics were fast, with 90% of the equilibrium capacity reached within approximately 9 to 11 min, and the pseudo-second-order behavior consistent with the chemisorption-controlled uptake. A dedicated N_2 experiment at 20 °C yielded a CO_2 to N_2 selectivity between approximately 74 and 97 across the 100 to 1000 mbar window, confirming negligible N_2 competition. A dual-site Langmuir model with shared site capacities of 1.87 and 1.70 mmol/g describes the three absolute isotherms with $R^2 \geq 0.997$. The measured working capacities range from 0.45 to 0.85 mmol/g for a 1000 to 100 mbar swing and reach 2.1 mmol/g for a 30 to 1 bar swing at 20 °C. These results establish the equilibrium bounds, cyclic robustness, and kinetic behavior of this benchmark resin across a wide condition window and provide the sorbent-level dataset required for isotherm model fitting and process design of sub-atmospheric and elevated-pressure CO_2 separation applications, while demonstration under dilute and humid feed conditions is left to dynamic breakthrough evaluation. Future work will examine the working behavior of the material in a fixed bed under realistic feed compositions, humidity, and regeneration atmospheres.

Supplementary Materials: The following supporting information can be downloaded at https://www.mdpi.com/article/10.3390/separations13110346/s1, Figure S1: P&I diagram of IsoSORP (400-150,S-G) MSB, Figure S2: BET equipment in the lab, Figure S3: Buoyancy results example using He gas, Figure S4: Cyclability test of adsorption-desorption of CO_2 by the tested material. Cycles 17 and 18 were dedicated for adsorption-desorption kinetics study of CO_2 gas in this material. For this reason, the measuring points were 0, 1000, and 0 mbar. Usually, kinetics analysis evaluates how much the process pace is. This helps to understand and optimize the scale up of the process. Table S1: Isotherm tabular report of BET for the three ports.

Author Contributions: Conceptualization, M.A. and S.A.; methodology, M.A. and A.M.R.A.-B.; software, A.M.R.A.-B., A.G.V. and M.A.; validation, A.M.R.A.-B., N.K. and M.A.; formal analysis, A.M.R.A.-B., S.A., A.G.V. and M.A.; investigation, A.M.R.A.-B. and M.A.; resources, M.A.; data curation, A.M.R.A.-B., N.K. and M.A.; writing—original draft preparation, A.M.R.A.-B. and M.A.; writing—review and editing, M.A.; visualization, A.M.R.A.-B., N.K. and M.A.; supervision, M.A.; project administration, M.A.; funding acquisition, M.A. All authors have read and agreed to the published version of the manuscript.

Funding: This research was funded by the U.S. Department of Energy (DOE) Office of Critical Minerals and Energy Innovation (CMEI) (formerly the Office of Energy Efficiency and Renewable Energy [EERE]) under Contract No. DE-FE0032521.

Data Availability Statement: Data is contained within the article or Supplementary Material.

Conflicts of Interest: The authors declare no conflicts of interest.

Abbreviations

The following abbreviations are used in this manuscript:

Carbon Dioxide	CO_2
Nitrogen	N_2
Intergovernmental Panel on Climate Change	IPCC
Direct Air Capture	DAC
Electrochemically Mediated CO_2 Capture	EMCC

Metal–Organic Frameworks	MOFs
Magnetic Suspension Balance	MSB
Helium	He
Safety Data Sheet	SDS
Thermogravimetric Analysis	TGA
Fourier Transform Infrared Spectroscopy	FTIR
Brunauer–Emmett–Teller	BET
Scanning Electron Microscopy	SEM
Gas-Dosing System	GDS
Derivative Thermogravimetry	DTG
Onset Temperature	T_{onset}
Maximum Degradation Temperature	T_{maxt}
Methylene	CH_2
Energy-Dispersive X-Ray Spectroscopy	EDS
Dual-Site Langmuir	DSL
Root Mean Square Error	RMSE
Average Absolute Relative Deviation	AARD
Isothermal Hysteresis	Δq
Isosteric Heat of Adsorption	Q_{st}
The Universal Gas Constant	R

References

1. Al-Bodour, A.; Alomari, N.; Gutiérrez, A.; Aparicio, S.; Atilhan, M. Exploring the thermophysical properties of natural deep eutectic solvents for gas capture applications: A comprehensive review. *Green Chem. Eng.* **2024**, *5*, 307–338. [CrossRef]
2. Hu, Y.; Li, X.; Zhou, T. Direct air capture: Recent progress in materials, equipment, and process engineering. *Curr. Opin. Chem. Eng.* **2025**, *50*, 101197. [CrossRef]
3. Hanna, R.; Abdulla, A.; Xu, Y.; Victor, D.G. Emergency deployment of direct air capture as a response to the climate crisis. *Nat. Commun.* **2021**, *12*, 368. [CrossRef] [PubMed]
4. Lackner, K.; Ziock, H.-J.; Grimes, P. Carbon Dioxide Extraction from Air: Is It An Option? Los Alamos National Lab., NM (US). 1999. Available online: https://www.osti.gov/biblio/770509 (accessed on 27 January 2026).
5. Sanz-Pérez, E.S.; Murdock, C.R.; Didas, S.A.; Jones, C.W. Direct Capture of CO_2 from Ambient Air. *Chem. Rev.* **2016**, *116*, 11840–11876. [CrossRef] [PubMed]
6. Keith, D.W.; Holmes, G.; Angelo, D.S.; Heidel, K. A Process for Capturing CO_2 from the Atmosphere. *Joule* **2018**, *2*, 1573–1594, Correction in *Joule* **2018**, *2*, 2179. [CrossRef]
7. Hu, Y.; Sun, L.; Zhou, T. Multiscale process systems engineering for electrochemically mediated CO_2 capture: A mini-review. *Chem. Eng. Sci.* **2025**, *307*, 121340. [CrossRef]
8. Ye, Z.-M.; Xie, Y.; Kirlikovali, K.O.; Xiang, S.; Farha, O.K.; Chen, B. Architecting Metal–Organic Frameworks at Molecular Level toward Direct Air Capture. *J. Am. Chem. Soc.* **2025**, *147*, 5495–5514. [CrossRef] [PubMed]
9. Sriram, A.; Choi, S.; Yu, X.; Brabson, L.M.; Das, A.; Ulissi, Z.; Uyttendaele, M.; Medford, A.J.; Sholl, D.S. The Open DAC 2023 Dataset and Challenges for Sorbent Discovery in Direct Air Capture. *ACS Cent. Sci.* **2024**, *10*, 923–941. [CrossRef] [PubMed]
10. Le Quéré, C.; Andres, R.J.; Boden, T.; Conway, T.; Houghton, R.A.; House, J.I.; Marland, G.; Peters, G.P.; van der Werf, G.R.; Ahlström, A.; et al. The global carbon budget 1959–2011. *Earth Syst. Sci. Data* **2013**, *5*, 165–185. [CrossRef]
11. Low, M.-Y.A.; Barton, L.V.; Pini, R.; Petit, C. Analytical review of the current state of knowledge of adsorption materials and processes for direct air capture. *Chem. Eng. Res. Des.* **2023**, *189*, 745–767. [CrossRef]
12. Rajagopalan, A.K.; Avila, A.M.; Rajendran, A. Do adsorbent screening metrics predict process performance? A process optimisation based study for post-combustion capture of CO_2. *Int. J. Greenh. Gas. Control* **2016**, *46*, 76–85. [CrossRef]
13. Khurana, M.; Farooq, S. Adsorbent Screening for Postcombustion CO_2 Capture: A Method Relating Equilibrium Isotherm Characteristics to an Optimum Vacuum Swing Adsorption Process Performance. *Ind. Eng. Chem. Res.* **2016**, *55*, 2447–2460. [CrossRef]
14. Farmahini, A.H.; Krishnamurthy, S.; Friedrich, D.; Brandani, S.; Sarkisov, L. Performance-Based Screening of Porous Materials for Carbon Capture. *Chem. Rev.* **2021**, *121*, 10666–10741. [CrossRef] [PubMed]
15. Bos, M.J.; Pietersen, S.; Brilman, D.W.F. Production of high purity CO_2 from air using solid amine sorbents. *Chem. Eng. Sci. X* **2019**, *2*, 100020. [CrossRef]
16. Veneman, R.; Frigka, N.; Zhao, W.; Li, Z.; Kersten, S.; Brilman, W. Adsorption of H_2O and CO_2 on supported amine sorbents. *Int. J. Greenh. Gas. Control* **2015**, *41*, 268–275. [CrossRef]
17. Buijs, W.; de Flart, S. Direct Air Capture of CO_2 with an Amine Resin: A Molecular Modeling Study of the CO_2 Capturing Process. *Ind. Eng. Chem. Res.* **2017**, *56*, 12297–12304. [CrossRef] [PubMed]

18. Alesi, W.R., Jr.; Kitchin, J.R. Evaluation of a Primary Amine-Functionalized Ion-Exchange Resin for CO_2 Capture. *Ind. Eng. Chem. Res.* **2012**, *51*, 6907–6915. [CrossRef]
19. Yu, Q.; Delgado, J.d.l.P.; Veneman, R.; Brilman, D.W.F. Stability of a Benzyl Amine Based CO_2 Capture Adsorbent in View of Regeneration Strategies. *Ind. Eng. Chem. Res.* **2017**, *56*, 3259–3269. [CrossRef] [PubMed]
20. Sonnleitner, E.; Schöny, G.; Hofbauer, H. Assessment of zeolite 13X and Lewatit® VP OC 1065 for application in a continuous temperature swing adsorption process for biogas upgrading. *Biomass Convers. Biorefin.* **2018**, *8*, 379–395. [CrossRef]
21. Chimani, F.M.; Bhandari, A.A.; Wallmüller, A.; Schöny, G.; Müller, S.; Fuchs, J. Evaluation of CO_2/H_2O Co-Adsorption Models for the Anion Exchange Resin Lewatit VPOC 1065 under Direct Air Capture Conditions Using a Novel Lab Setup. *Separations* **2024**, *11*, 160. [CrossRef]
22. Low, M.-Y.A.; Danaci, D.; Azzan, H.; Woodward, R.T.; Petit, C. Measurement of Physicochemical Properties and CO_2, N_2, Ar, O_2, and H_2O Unary Adsorption Isotherms of Purolite A110 and Lewatit VP OC 1065 for Application in Direct Air Capture. *J. Chem. Eng. Data* **2023**, *68*, 3499–3511. [CrossRef] [PubMed]
23. Alomari, N.; Al-Bodour, A.; Khai Liew, S.; Gutiérrez, A.; Aparicio, S.; Atilhan, M. Exploiting monoterpenoids in type V deep eutectic solvents: A combined high-pressure experiments and theoretical approach for enhanced carbon dioxide and nitrogen absorption. *J. Mol. Liq.* **2023**, *391*, 123267. [CrossRef]
24. Cavenati, S.; Grande, C.A.; Rodrigues, A.E. Adsorption Equilibrium of Methane, Carbon Dioxide, and Nitrogen on Zeolite 13X at High Pressures. *J. Chem. Eng. Data* **2004**, *49*, 1095–1101. [CrossRef]
25. Millward, A.R.; Yaghi, O.M. Metal−Organic Frameworks with Exceptionally High Capacity for Storage of Carbon Dioxide at Room Temperature. *J. Am. Chem. Soc.* **2005**, *127*, 17998–17999. [CrossRef] [PubMed]
26. Caskey, S.R.; Wong-Foy, A.G.; Matzger, A.J. Dramatic Tuning of Carbon Dioxide Uptake via Metal Substitution in a Coordination Polymer with Cylindrical Pores. *J. Am. Chem. Soc.* **2008**, *130*, 10870–10871. [CrossRef] [PubMed]
27. Xu, X.; Song, C.; Andresen, J.M.; Miller, B.G.; Scaroni, A.W. Novel Polyethylenimine-Modified Mesoporous Molecular Sieve of MCM-41 Type as High-Capacity Adsorbent for CO_2 Capture. *Energy Fuels* **2002**, *16*, 1463–1469. [CrossRef]
28. Serna-Guerrero, R.; Belmabkhout, Y.; Sayari, A. Modeling CO_2 adsorption on amine-functionalized mesoporous silica: 1. A semi-empirical equilibrium model. *Chem. Eng. J.* **2010**, *161*, 173–181. [CrossRef]
29. Al-Bodour, A.; Alomari, N.; Aparicio, S.; Atilhan, M. A comprehensive study on carbon capture potential of lactic acid based deep eutectic solvents at wide process conditions. *J. Mol. Liq.* **2023**, *390*, 123114. [CrossRef]

Disclaimer/Publisher's Note: The statements, opinions and data contained in all publications are solely those of the individual author(s) and contributor(s) and not of MDPI and/or the editor(s). MDPI and/or the editor(s) disclaim responsibility for any injury to people or property resulting from any ideas, methods, instructions or products referred to in the content.